Dynamics of light-induced charge transfer between carbon nanotube and CdSe/CdS core/shell nanocrystals

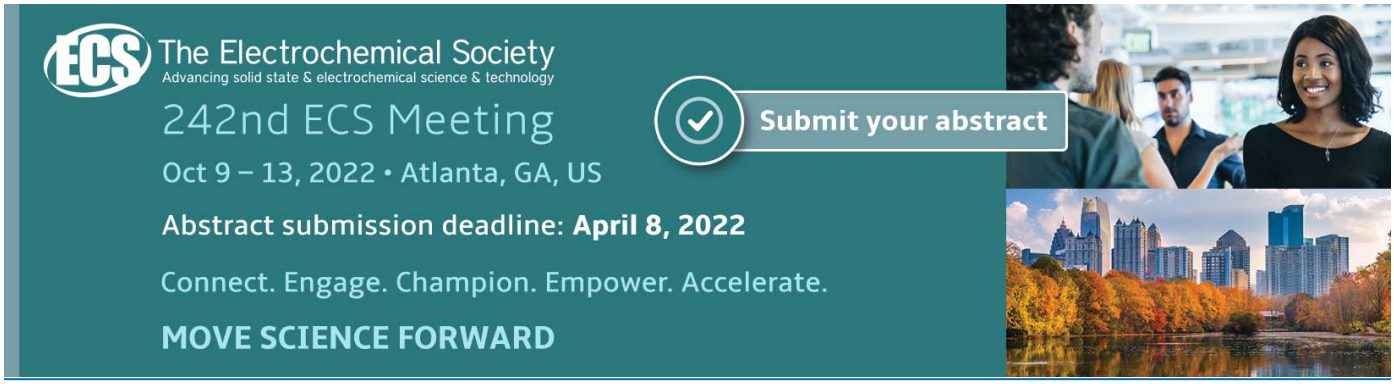

IOP Publishing Nano Futures 6 (2022) 015001 https://doi.org/10.1088/2399-1984/ac3ccc

NANO FUTURES

PAPER

Dynamics of light-induced charge transfer between carbon nanotube and CdSe/CdS core/shell nanocrystals

Gilad Zeevi[1], Joanna Dehnel[2,4], Adam K Budniak[2,4], Yana Milyutin[3], Guy Ankonina[4], Hossam Haick[3,4], Efrat Lifshitz[2,4] and Yuval E Yaish[1,4,*]

[1] Andrew and Erna Viterbi Faculty of Electrical and Computer Engineering, Technion, Haifa 3200003, Israel
[2] Schulich Faculty of Chemistry, Solid State Institute, Technion, Haifa 3200003, Israel
[3] Department of Chemical Engineering Technion, Haifa 3200003, Israel
[4] Russell Berrie Nanotechnology Institute, Technion, Haifa 3200003, Israel
[*] Author to whom any correspondence should be addressed.

E-mail: yuvaly@technion.ac.il

Keywords: CdSe/CdS core/shell nanocrystals, seeded nanorods, CNTFET, charge transfer, carbon nanotube

Supplementary material for this article is available online

RECEIVED
25 August 2021

REVISED
21 November 2021

ACCEPTED FOR PUBLICATION
23 November 2021

PUBLISHED
20 January 2022

Abstract

The integration of semiconducting colloidal nanocrystals (NCs) with carbon nanotubes (CNTs) in a single device presents a unique platform that combines optical flexibility with high charge carrying capability. These qualities are desirable in many applications such as photovoltaic cells, photocatalysis, and light sensors. Here, we present hybrid devices that incorporate various CdSe/CdS core/shell NCs, such as seeded quantum dots and asymmetric seeded nanorods (a-sNRs), with a single-wall CNT in a field-effect transistor geometry. We used electrical measurements to probe a light-induced charge transfer (LICT) between the CdSe/CdS NCs and the CNT. We investigate the effect of gate voltage on the LICT magnitude and temporal characteristics. Surprisingly, the measured photo-response depends on the gate voltage, and we observe both electrons and holes transfer from the a-sNRs to the CNT. Furthermore, a comparison between LICT measurements on different devices with different CNTs and NC types reveals that the charge transfer time is directly proportional to the shell-thickness around the CdSe core and inversely correlated with the NCs size. The recovery of the charge trapped inside the CdSe/CdS NCs is characterized by two distinct fast and slow relaxation times, which depend on the NCs size and CNT type. Although, the charge relaxation time is similar between the symmetric QDs and the asymmetric sNRs, the overall percentage of the remaining charge in the QDs is significantly larger than in the sNRs. Understanding both gate voltage and NCs size effect on the LICT processes can optimize the performance of optoelectronic devices.

1. Introduction

The mixing of two building blocks from two different fields can result in a complementary behavior that in many instances, would enhance and improve their individual functionalities. Such a promising combination includes the pairing of carbon nanotubes (CNTs) and semiconducting nanocrystals (SC-NCs). On one side, CNTs display a large current-carrying capability, high mobility, exceptional tensile strength, and thermal properties [1]. On the other side, SC-NCs allow for large flexibility and efficient controllability of their bandgap as well as an excellent optical response [2–4]. These qualities are enhanced in heterostructures of seeded NCs that consist of more than a single component [5, 6]. For example, seeded nanorods (sNRs) in photovoltaic devices and photodetectors have exhibited a highly efficient charge separation [7–11]. The combination of the high charge transport capabilities of CNTs with the optoelectronic flexibility of single component symmetric quantum dots (QDs) was studied for light-harvesting applications such as photovoltaic cells [12–18], photocatalysis [19, 20], and light sensors [21–30]. Equivalently, Konstantatos *et al* [31] reported a large responsivity $\sim 10^7$ A W^{-1} and photoconductive gain $\sim 10^8$ in an analogous hybrid device comprised graphene and colloidal QDs.

A major factor in the efficiency of such devices is the charge transfer (CT) between the SC-NCs and the CNT. Hybrid CNT-NCs devices are driven by a light-induced CT (LICT), where a photon is absorbed by the NC, forming an exciton, followed by a charge disassociation. Due to the band structure of the CNT-NCs hybrid, often it is the electron being collected by the CNT leaving a positively charged NC. Most previous research on the LICT between CNTs and semiconductor-NCs has included a single element of NCs, usually shaped as QDs or elongated NRs. Opposite results on the relation between the CdSe-QDs' diameter and the amount of LICT involving single or double-wall CNT (DWCNT), while trapping the hole via 4-mercaptophenol (MTH) linker was reported [32, 33]. Wang *et al* [32] found from x-ray absorption fine structure (NEXAFS) measurements and Raman spectroscopy an inverse relation between CdSe QDs' diameter and the CT magnitude. This contrasted with a direct relation they extracted from electrical measurements, indicating a possible denser coverage of CNTs surfaces upon the use of the larger QDs. Zhu *et al* [33] further estimated the LICT magnitude between CNT and CdSe QDs by calculating the LICT as a function of the difference in the gate-voltage at the minimum-conduction point (Dirac point) for CNTs with and without illumination. The calculations estimated a CT of ≈300 electrons μm^{-1} for approximate density of 1000 QDs·μm^{-1} (laser−488 nm @98 nW). Other CNT-NCs combinations include a single-wall CNT (SWCNT) ensemble (mesh on substrate or solution) with NCs adhered to the CNTs by van der Waals forces [21, 34], where the charge separation of excited electron-hole pair results in electron transfer to the CNTs, while the hole stays trapped in the NCs. The LICT was demonstrated either by the difference in drain-source current between periods of illumination and darkness [21] or by a blue shift in the absorbance spectrum [34]. For devices having a field-effect transistor (FET) geometry, an initial CT appears in NCs decorated CNTs (compared to pristine CNTs) even before a light source was applied [32, 35]. This CT originates from the difference in the work functions and energy bands alignment between the device's constituents, causing either an electrons migration from the NCs into the CNT causing n-doping of the CNT, or modifying the Schottky barrier between the CNT and the source and drain contacts. Another aspect of the LICT between a SWCNT and the NCs is the CT rate. By using single-molecule spectroscopy combined with time-correlated single-photon counting, Chi-Tsu Yuan *et al* [7] measured electron transfer rates between a SWCNT and a single core/shell NC. They found LICT rate of $\sim 10^8$ s^{-1} between type-I CdSe/ZnS QDs (or CdSe/CdS sNRs) to SWCNTs, and even larger LICT ($\sim 10^9$ s^{-1}) for type-II, ZnSe/CdS sNRs. Similar CT rates were measured by the fluorescence decay measurements technique between CNT-mesh and SC-NCs [34, 36]. These results are in sharp contrast to the temporal characteristics of photo-response obtained by direct electrical measurements, which have typical time scales of 10^{-2}–10^2 s [21, 35, 37]. Both charge and energy transfer are frequently intertwined with each other. The discrepancy in the temporal characteristics may originate from the difficulty of unambiguously determining the dominance of one process over the other and will be further discussed in the main text.

The current study concentrates on gate-voltage dependence of CT between SWCNT and asymmetric CdSe/CdS core-shell sNRs and compares it to symmetric CdSe/CdS core–shell QDs. We predominantly utilize a single, small bandgap CNTs (with ambipolar conductance) in a FET configuration, where the core/shell NCs are drop-casted on top of the CNTs. The lack of any FET surface preparation or resist residues that adhere to the CNT should facilitate the CT. We measure the device transfer characteristics (I_{DS} vs V_{GG}) and I_{DS} vs time under different gate voltages (V_{GG}) and illumination conditions, to reveal the mechanism of the LICT processes. Attempting to extract temporal dependence of the LICT parameters directly from the I_{DS} vs time measurement is lacking, since it depends on both device's transfer characteristics and the charge trapped in the SC-NCs. To overcome this issue, we first convert the I_{DS} vs time measurements to V_{Dirac} vs time, where V_{Dirac} is the gate voltage at the Dirac point (minimum conductance point). We adapt physics-based dynamic models to fit the translated data and extract temporal and magnitude parameters that describe the LICT processes. Since the measurements are performed under fixed gate and bias voltages, any shift of V_{Dirac} (ΔV_{Dirac}) is directly associated with a charge trapped in the NCs. The conversion of ΔV_{Dirac} to trapped charges is carried out with a simple capacitive model. The research includes a comprehensive analysis of the influence of the NC's type and shapes on the LICT and retention efficiency, as well as a description of the LICT processes under different electrical stresses.

2. Device fabrication

Our devices share the basic structure of a typical CNTFET. We use a conventional E-beam lithography and lift-off processes to pattern a matrix of electrode-groups on top of a heavily p-doped silicon substrate with a thermal oxide (285 nm thick). The electrodes comprise Cr/Pt/Au—3/7/10 nm were deposited by E-beam evaporation. CNTs were grown from ferritin catalyst by chemical vapor deposition at 900 °C, using a gas mixture of hydrogen and methane under atmospheric pressure [38]. The grown CNTs were transferred on top of the metal electrodes, where each electrode-group (consists of five electrodes) shares the same CNT.

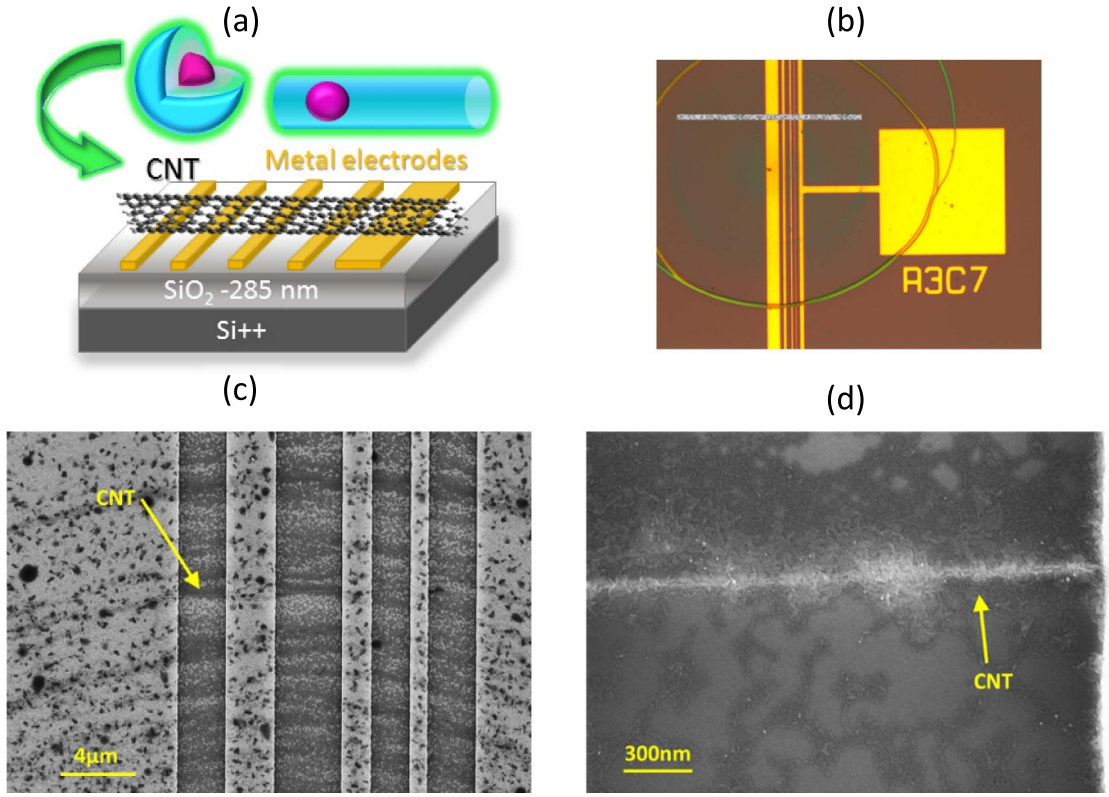

Figure 1. Fabricated hybrid CdSe/CdS-CNTFET Devices. (a) A schematic device configuration based on a cross-section of a CNT and the five-electrodes group with a layer of deposited NCs on top. (b) Optical microscope image of an electrodes-group covered with two droplets (0.3 nl) of sNRs_A in toluene solution. For convenience, a gray textured line represents the CNT that is already crossing the electrodes before the sNRs_A deposition. (c) SEM image of a CNT crossing the electrodes (marked by the yellow arrow). (d) SEM image of CNT crosses the channel between two electrodes. The sNRs_A are dispersed on top of the CNT and cover a large portion of the SiO_2 surface as well.

The final stage includes the deposition of a colloidal solution of NCs at the specific site on the device. We work with colloidal CdSe/CdS NCs varied in shape and size (seeded nanorods—sNRs or seeded quantum dots—sQDs). The NCs are stabilized by organic ligands and suspended in toluene. Details of the NCs synthesis are given in the supporting information (SI sections 2 and 3). The physical parameters of the NCs are summarized in table S2 (available online at stacks.iop.org/NANOF/6/015001/mmedia) of the SI and the absorption and photoluminescence (PL) spectra of CdSe/CdS sNRs_A recorded at room temperature [39] are presented in sections 4 and 5 of the SI. For the NCs deposition, we used an inkjet printing technology, sciFLEXARRAYER S3 dispenser system operated by SciFlex_s3 program with nozzle PDC 70 (Piezo Dispenser Capillary nozzle 70 μm) to drop one or two 0.3 nanoliter droplets of the NCs solution on top of each group of devices. The NCs adhere physically to the CNTs, electrodes, and SiO_2 surface via van der Waals forces. Figure 1(a), illustrates a cross-section of five electrodes on top of a Si/SiO_2 substrate, with a single CNT crossing all of them. We drop cast sNRs_A (see table S2 of the SI) droplets on the CNT. Figure 1(b) shows the top view (optical microscope image) of a set of five electrodes covered by sNRs_A (two droplets), the gray line represents the CNT which lies above the electrodes and beneath the sNRs. Figures 1(c) and (d) present a closer look (SEM image) on the CNT, sNRs_A, and electrodes.

3. Experimental methods

We explore the LICT in hybrid NCs-CNT devices in a CNTFET configuration. The study includes LICT under different gate voltage (V_{GG}) and illumination conditions, as well as charge retention at the end of the illumination period. We use LakeShore CRX-VF probe station, NI DAQ PCI-6621 for DC voltage sources and data sampling, SR570 as a low-noise current amplifier (for I_{DS}), and Agilent 33250A function generator for voltage pulses. The light source is a Halogen bulb EKE-SPC, 21 V 150 W with measured intensity of $\sim$2 mW cm^{-2} on the die surface (see figure S4 of the SI for light source spectra).

Our experiments consist of two main measurement procedures:

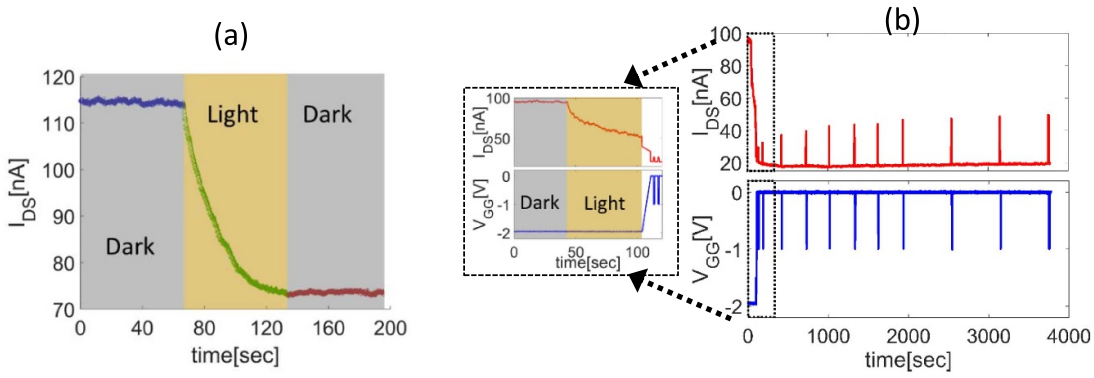

Figure 2. Measurements procedures with sNRs_A. (a) CT measurement. Temporal evolution of I_{DS} under fixed $V_{GG} = -2.1$ V and $V_{DS} = 10$ mV. During the first minute, the light is off, and the current is stable (blue I_{DS} segment). Next, the light is turned on for one minute and I_{DS} decreases in magnitude (green I_{DS} segment). Finally, the light is turned off again and the current remains stable for the rest of the measurement (red I_{DS} segment). (b) Charge retention. The top (bottom) panel depicts I_{DS} (V_{GG}) as a function of time. Left image: a zoom-in on the first 100 s, which includes I_{DS} measurement at $V_{GG} = 2$ V, with an initial short period (∼40 s) in the dark and subsequent 60 s of LICT (writing) stage where the light is turned on. The retention begins at the end of the charging stage when both the light is turned off and the V_{GG} goes to 0 V. The right panels depict the entire measurement sequence, where frequent V_{GG} pulses (−1 V@1 s) are used to read the I_{DS} value. $V_{DS} = 20$ mV throughout the entire measurement.

(a) CT measurements (figure 2(a)) for establishing the CT rate and magnitude under various V_{GG} conditions. This technique includes:
   1. 'Dark–light–dark' measurement sequence probes the NCs charging parameters. The source/drain current (I_{DS}) is measured under a fixed bias and V_{GG}. During the first minute, the light is off, and the I_{DS} stability is monitored for any CT processes related to the electrostatic stress from the gate voltage. Next, the device is exposed to a white light source for one minute. Then the light is turned off while I_{DS} is still measured for an additional one minute. This extra minute reveals charge recovery processes immediately after the illumination was turned off.
   2. Shortly after the measurement sequence described in 1. was finished, we measure the device's transfer characteristics under dark conditions and limited V_{GG} sweep range (±2 V). This method offers another view on the amount of charge that remains stored in the NCs, by direct probing of the deviation of the Dirac voltage (V_{Dirac}) or threshold voltage (V_{TH}) from their values measured for a pristine device (ΔV_{Dirac} or ΔV_{TH} respectively). This voltage shift gives a lower bound for the charge stored in the NCs at the end of the measurement described in 1. since even with the limited V_{GG} sweep range, there is a substantial charge recovery. However, these measurements provide an estimation for the amount of 'stable' charge (stable under limited V_{GG} range) trapped in the NCs.
   3. After each pair of measurements mentioned in 1. and 2., we make sure that the device returns as close as possible to its original (pristine) state, before beginning with the next set of measurements under different V_{GG}.

(b) Retention measurements (figure 2(b))—under constant V_{GG} and no light we measure I_{DS} for a period of a few tenths of seconds. Next, the light is turned on and we monitor the current for 1 min of LICT (still under the same constant V_{GG}). Finally, we simultaneously turn off the light and bring V_{GG} back to 0 V as the charge-retention stage begins. We measure the I_{DS} at $V_{GG} = 0$ V and frequently apply V_{GG} pulses ($V_{GG} = -1$ V@1 s) to read the I_{DS} state. The main panel of figure 2(b) shows a typical example of I_{DS} (top) and V_{GG} (bottom) vs time during such a measurement. The image on the left magnifies the beginning of the measurement and shows the initial dark period and the subsequent LICT interval.

Later, the evolution of I_{DS} is translated into the shift of the Dirac point voltage—ΔV_{Dirac}, for small bandgap CNT or shift of the threshold voltage—$\Delta V_{TH,}$ for SC-CNT (see figure S3 of the SI). The processed data are fitted to exponential dynamic equations, and the appropriate characteristic parameters such as decay time constants and amplitudes are extracted. Furthermore, the magnitude of the transferred/retained electrical charge is estimated.

4. Results and discussion

Prior to NCs deposition, we measure no effect of the illumination on the device's transfer characteristics. Similar results were obtained in a control experiment, where we drop-casted a solution consists of organic

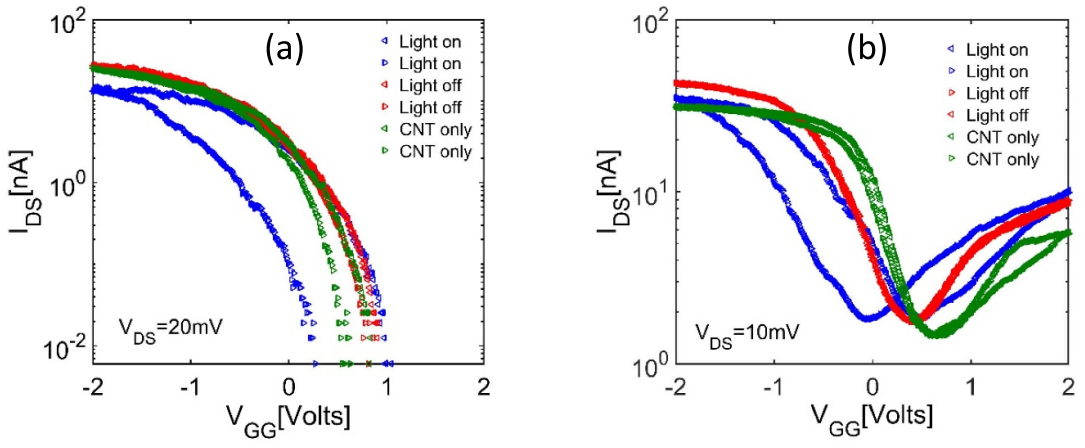

Figure 3. Effect of sNRs_A dispersion and illumination on the transfer characteristics. The images include measurements of V_{GG} sweeps in both directions (pointed by the direction of the triangles in the legend). The labels 'Light on', and 'Light off' correspond to turning the light 'on' and 'off' respectively, after sNRs deposition. (a) Semiconducting CNT. The measurements of the 'CNT only' and the 'Light off' are very similar. Turning the light on results with a hysteresis window. (b) Small bandgap CNT. Compared to the 'CNT only', the 'Light off' measurement presents a slight n-doping of the CNT and a small improvement in the contact resistance. As for the case of the SC-CNT, the 'Light on' measurement shows a substantial hysteresis window.

ligands (which have been used for coating the NCs) without the NCs. Figure 3 depicts the effect of sNRs_A deposition and subsequent illumination on the transfer characteristics of two distinct devices. Figure 3(a) presents the results of a semiconducting CNT (SC-CNT). The sNRs deposition itself seems to have almost no effect on the transfer characteristics (red symbols), while turning the light on opens a substantial hysteresis window (blue symbols). Figure 3(b), depicts the transfer characteristics of a small bandgap CNT. In this case, the sNRs deposition improved marginally the contact resistance and slightly n-doped the device (red symbols). Again, after turning the light on a hysteresis window is observed (blue symbols). The lack of hysteresis for devices with 'CNT only' (with or without illumination) or devices that include the sNRs but the light is off, suggests that the illumination is responsible for the observed response. We suggest that this effect is a photo-gating effect that originates from CT between the sNRs to the CNT (or possibly to nearby traps in the SiO_2 dielectric). One may expect that this LICT will depend both on the illumination properties (wavelength, duration, power, etc) as well as on the gate voltage which modifies the relative position of the sNR's and CNT's energy levels. Indeed, our findings support this hypothesis, and a clear difference behavior is observed for positive and negative gate voltages, as will be discussed shortly.

4.1. Charge transfer

To measure the LICT between the sNRs and the CNTs we use two different types of measurements: (a) the CNT's transfer characteristics curve (I_{DS} vs V_{GG}), as well as (b) the I_{DS} vs time. These measurements were performed under different electrical stress (V_{GG}) and environmental conditions (N_2 atmosphere and vacuum). The dynamics of the I_{DS} during the illumination period are translated into the temporal dependence of the voltage shift of the Dirac point (ΔV_{Dirac}) (see figure S3 of the SI). Then, we analyze the temporal development of ΔV_{Dirac} according to a single exponential kinetic equation, equation (1):

$$\mathrm{Fit}_1 = C_1 \cdot \left(1 - e^{-\left(t/\tau_1\right)}\right) \tag{1}$$

where C_1 corresponds to the final ΔV_{Dirac} shift and τ_1 is the characteristic relaxation time. Under the assumption that CT occurs from the sNRs which are either in direct contact with the CNT (first layer) or the ones that are connected to them (second layer), we model the sNRs assembly as an effective single nanowire with a diameter equal to twice the diameter of a single sNR. Therefore, the ΔV_{Dirac} is translated into CT by a capacitive model:

$$\begin{aligned} \mathrm{CT} &= \Delta Q = C_{NR} \cdot \Delta V_{Dirac} \\ C_{NR} &\approx \frac{2\pi\varepsilon_0\varepsilon_{SiO2}}{\ln\left(2D_{SiO2}/d_{NR}\right)} \approx 43\,aF \cdot \mu\mathrm{m}^{-1} \end{aligned} \tag{2}$$

where C_{NR} is the capacitance between the gate and the effective NR wire, $\varepsilon_0 = 8.85 \times 10^{-18}$ F $\mu\mathrm{m}^{-1}$ is the permittivity of free space, $\varepsilon_{SiO2} = 3.9$ is the relative SiO_2 permittivity, $D_{SiO2} = 285$ nm is the SiO_2 thickness, and $d_{NR} = 4$ nm is the NR diameter.

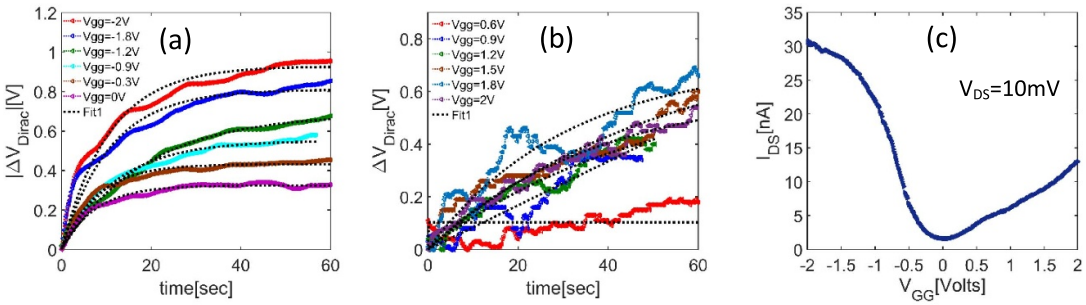

Figure 4. Temporal evolution of $\Delta V_{\mathrm{Dirac}}$ during illumination at various electrical stresses (for different V_{GG} as signed in the figure legend). The colored curves represent $|\Delta V_{\mathrm{Dirac}}|$ data that were extracted from the ΔI_{DS} as described in the text. (a) For negative V_{GG} the $\Delta V_{\mathrm{Dirac}}$ is negative. To ease the comparison to the measurements under positive V_{GG}, the image presents $|\Delta V_{\mathrm{Dirac}}|$. Fit_1 (dashed dark line) represents the fitting of the various measurements to equation (1). (b) Same as (a) but for positive V_{GG}. (c) The device's transfer characteristics (in the dark) before any LICT measurement. At $V_{\mathrm{Dirac}} \approx 0$ V the majority carriers in the CNT change from holes (negative V_{GG}) to electrons (positive V_{GG}).

Figure 4 displays a set of $\Delta V_{\mathrm{Dirac}}$ vs time measurements performed on a sNRs_A-CNT device, under N_2 atmosphere at room temperature (see figure S3 of the SI for a typical raw data of I_{DS} vs time). Figure 4(a) presents $|\Delta V_{\mathrm{Dirac}}|$ vs time during the 60 s of illumination, under various negative V_{GG} values. For negative V_{GG} measurements, the $\Delta V_{\mathrm{Dirac}}$ is negative since the excited electrons are ejected from the sNRs to the CNT and leave a positively charged sNRs, which n-dope the CNT. The $|\Delta V_{\mathrm{Dirac}}|$ data grow monotonously with time, seem to (almost) saturate after 60 s and show satisfactory agreement to equation (1). Figure 4(b), depicts similar measurements performed under positive V_{GG}. Unlike the data for $V_{\mathrm{GG}} < 0$, for positive V_{GG} the data fluctuate and show non-monotonous behavior. For low positive V_{GG} in the range of ~0.3 to 0.9 V there is no obvious CT or significant $\Delta V_{\mathrm{Dirac}}$. For V_{GG} larger than 0.9 V the $\Delta V_{\mathrm{Dirac}}$ is positive and tends to increase with time. However, it is very noisy, does not saturate after the 60 s of illumination, and shows poor agreement with equation (1). Figure 4(c) depicts the device's transfer characteristics, acquired with no light, before any LICT measurements were performed. These data were used as a reference to translate the ΔI_{DS} vs time to $\Delta V_{\mathrm{Dirac}}$ vs time. The I_{DS} curve shows ambipolar conductivity, where holes or electrons are the majority carriers for $V_{\mathrm{GG}} < 0$ V and $V_{\mathrm{GG}} > 0$ V, respectively.

However, the transfer characteristics by themselves cannot explain the differences of $|\Delta V_{\mathrm{Dirac}}|$ between negative and positive V_{GG}. We propose that the LICT between the CdSe/CdS sNRs and the CNT also depends on the energy band alignment between the three constituents (CdSe seed, CdS shell, and the CNT). Figure 5 presents a model for the device's band alignment for different gate voltages. The model considers the small bandgap CNT as a semi-metal and presents most of the band bending at the CNT/sNRs interface inside the sNR due to its lower density of states (DOS) compared to the CNT. This band bending is possible due to the finite length and/or asymmetry of the core/shell sNRs. Figure 5(a) presents the band alignment at equilibrium ($V_{\mathrm{GG}} = 0$ V, dark). The band bending reflects a small accumulation of holes in the sNRs side, in agreement with the initial slight n-doping in our observations (the parameters for the CdSe/CdS sNRs energy bands were taken from Eshet *et al* [8]). The sNRs discussed here possess a type I band alignment, with relative deep potential well for holes (~35 meV) and shallow potential well for electrons (~10 meV), located in the CdSe seed (QD core). After illumination similar LICT processes happen for both $V_{\mathrm{GG}} = 0$ V and negative V_{GG}. Both electrons and holes are excited in the CdSe core and CdS shell. Those created in the shell can diffuse towards the CNT, the CdSe core, or fill a trap in the shell [40]. For the excited electron-hole pairs in the CdSe seed, the hole wave function is localized at the CdSe where the electron wave function is more delocalized and spread further into the shell region [41–43]. Figure 5(b) depicts an illustration of the energy band alignment at $V_{\mathrm{GG}} = -2$ V. As the V_{GG} becomes more negative, the band bending at the CNT/CdS interface promotes the electron transfer and reduces the hole transfer to the CNT. The excited electrons tunnel more easily from the sNR into the CNTs conduction band (CB), and quickly recombine with holes (majority carrier in the CNT) or manage to be collected by the contacts. We entitle this LICT as 'negative LICT', due to a negative CT from the sNRs to the CNT (leaving the sNRs positively charged). For LICT under positive V_{GG} the situation is more complex. For low positive V_{GG} ($V_{\mathrm{GG}} < 0.9$ V), the electrons are the majority carriers in the CNT, however, the total CT is close to zero (in some devices we could even measure small negative LICT at these V_{GG} values). This behavior arises since the CNT's CB is still lower than the CB of the sNRs. As V_{GG} increases and becomes more positive, the bands of the sNRs and the CNT bends downward (not evenly due to the difference in their DOS) until both CBs align. First, there is an alignment between the CNT and the CdSe seed, and later for larger V_{GG}, the CBs of the CdS and the CNT align.

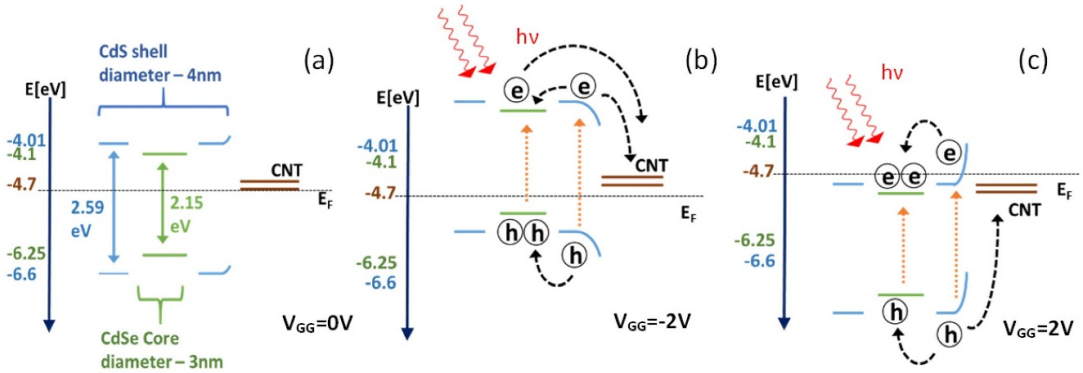

Figure 5. A model for the energy bands alignment at the CNT-sNR heterojunction and LICT processes under different V_{GG}. The Fermi energy (E_F) is kept constant by the source/drain electrodes, while the conductance and valance bands shift according to the field-effect caused by the gate voltage (V_{GG}). (a) $V_{GG} = 0$ V. The energy band alignment is at equilibrium. The blue lines represent the valance (VB) and conduction (CB) bands of the CdS shell, the green lines represent the VB and CB of the CdSe core, and the brown lines depict the VB and CB of a small bandgap CNT. The band bending at the CdS/CNT is modeled as a Schottky barrier, where the CNT acts as a semi-metal. The estimated values of the CdSe/CdS energy bands [8] are marked on the vertical axis, with the corresponding colors. (b) At $V_{GG} = -2$ V, both the CNT's and sNR's energy bands are shifted to higher energy. The predominant LICT processes (which are explained in the text) are depicted by black dashed arrows. The total LICT results in positively charged sNRs. (c) At $V_{GG} = 2$ V, due to the new band alignments and band bending at the sNRs/CNT heterojunction, the LICT processes results in negatively charged sNRs.

Figure 5(c) presents the energy band alignment at $V_{GG} = 2$ V. This LICT (for high enough V_{GG}) is a 'positive LICT', where the total charge transferred from the sNRs to the CNT is positive, as evident from the observed positive ΔV_{Dirac} (figure 4(b)). Under large positive V_{GG} the energy bands shift and an energy barrier at the CB between the sNRs and the CNT is formed. The excited electrons generated in the CdSe seed find it more difficult to hope to the CNT, and only a minority of electrons with high enough energy do manage to do so. In the CdS shell the holes diffuse equally to the CdSe seed and the CNT (in the absence of an energy barrier at the CNT/CdS junction). Excited electrons are predominantly diffuse to the CdSe seed, due to the energy barrier at the CdS/CNT junction. These two oppositely CT processes result in a total negative charge in the CdSe seed (and/or CdS traps) however this charge accumulation dynamic is much more random.

The description of band bending (or E_F shift) presented in figure 5 is based on the large difference of the DOS near E_F between the SC-sNR (inside its band gap) in comparison to the small bandgap CNT. The coupling between E_F and the gate voltage is given by:

$$\delta E_F = e \cdot \frac{C_G}{C_G + C_Q} \delta V_{GG} \tag{3}$$

where $e = |e|$ is the elementary charge of the electron, and C_G and C_Q are the geometrical and quantum capacitances per unit length, respectively. C_G is taken to be constant, while C_Q may vary considerably as a function of energy around E_F. For a one-dimensional (1D) system C_Q is described as:

$$C_Q = \frac{dq}{dV} = \frac{1}{L} \frac{\delta Q}{\delta (E/e)} = e^2 g(E) \tag{4}$$

where L is the capacitor length, Q is the total charge and $g(E)$ is the DOS per unit energy and length. From equation (3) we find that if $C_Q \ll C_G$, E_F changes significantly with V_{GG}, but on the other hand for $C_Q \gg C_G$, this change is very small. Since the DOS inside the bandgap is minuscule, equation (4) predicts a very small C_Q, which grows considerably at the bandgap edges. Therefore, the sNR's energy bands bend much more than those of the CNT under V_{GG} stresses, as depicted in figures 5(b) and (c).

Next, we analyze the temporal behavior of the LICT process. Figure 6(a) depicts the parameters extracted from fitting equation (1) to the data presented in figure 4. For negative V_{GG}, the temporal characteristics of the LICT change very little for different V_{GG} and $\tau_1 \approx 10$ s. On the other hand, the CT magnitude, C_1 increases almost linearly as a function of $|V_{GG}|$.

For positive V_{GG} the raw data fluctuate and show non-monotonous behavior, hence, the fittings based on equation (1) lose much of their validity, especially at the V_{GG} range of 0.3–0.9 V, where the LICT changes from negative LICT at negative V_{GG}, to positive LICT for V_{GG} larger than 1 V. Qualitatively, for $V_{GG} > 1$ V we see a clear tendency for higher CT and even larger time constant. We concentrate on the LICT under negative V_{GG}, where the quality of the fitting allows for more accurate analysis. Figure 6(b) depicts the

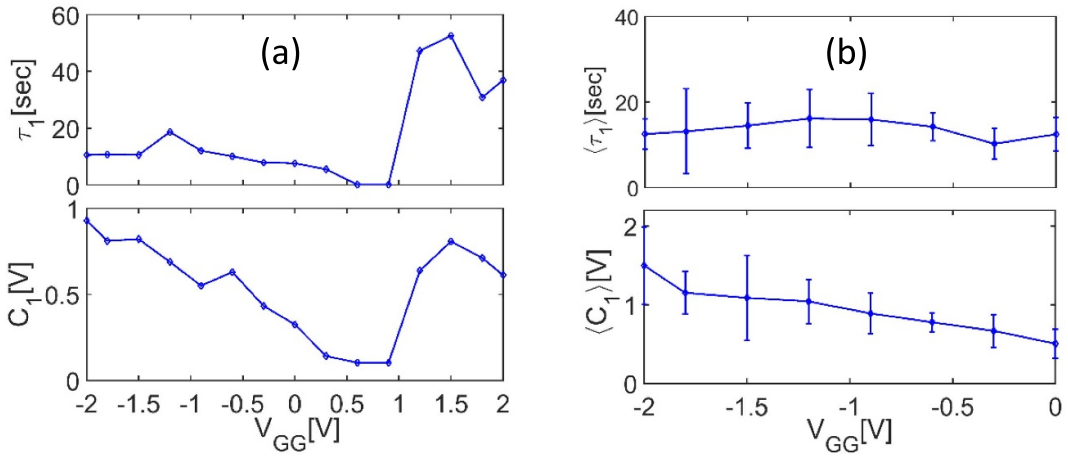

Figure 6. Fitting parameters as a function of the applied gate voltage, V_{GG}, during the LICT measurement. (a) Temporal characteristics—τ_1 (top panel) and the final absolute shift of the Dirac voltage—C_1 (bottom panel) parameters, extracted from fitting the data presented in figure 4 to equation (1). (b) $<C_1>$ and $<\tau_1>$ averages of five different devices (all comprise CNT and sNRs_A) for negative gate voltages. Error bars depict the standard deviation of the whole data set.

averages $\langle C_1 \rangle$ and $\langle \tau_1 \rangle$ extracted from a set of five measurements on different devices comprise sNRs_A and CNTs. The error bars display the standard deviation, and their size reflects the inhomogeneous of the sNRs dispersion as well as the different CNTs (all small bandgap CNTs) in the various devices. Nevertheless, qualitatively the data resemble the ones described in figure 6(a), where $\langle \tau_1 \rangle$ varies little with V_{GG} ($\langle \tau_1 \rangle \approx 13$s), while $\langle C_1 \rangle$ increases (almost) linearly with the $|V_{GG}|$ magnitude. These temporal characteristics agree very well with previous publications of CT using direct electrical measurement [21, 35, 37], however, they are much longer than time constants found in fluorescence decay measurements [7, 36, 44, 45].

In the electrical measurement of photo-response the I_{DS} modulations can result from two main sources:

(a) Photo-generated charge (electron or holes) transferred from the NCs to the CNT. These charges may recombine with the majority carriers in the CNT (I_{DS} reduction) or be collected by the S/D electrodes.
(b) Photo-gating: after CT is taking place, the charged NCs (which are in very close proximity to the CNT) effectively change the gate voltage or the electrostatic environment sensed by the CNT (causing Dirac-point ΔV_D or threshold voltage ΔV_{TH} shifts).

If we consider a CNTFET with a single CNT (2 nm diameter), and SiO_2 gate oxide of 300 nm thick, one finds geometrical gate capacitance of $C_G \sim 40$ aF μm^{-1}. The resulted shift of the Dirac voltage is given by the following expression: $\Delta V_{Dirac} = \Delta Q / C_{GG}$. Hence, a density of ~250 electrons (or holes) per 1 μm trapped close to the CNT will cause $\Delta V_{Dirac} \sim 1$ V. The ΔI_{DS} depends on the transfer characteristics slope at the working point (V_{GG} value) in which the photo-response was measured. The main point is that the photo-gating effect is specifically sensitive to the net CT between the SC-NCs and the CNT, and in our measurement is dominant. The large difference between our results and fast decay in fluorescence intensity measurements may be explained in the following way: CNTs typically report low quantum yields which indicate that more than 90% of the energy absorbed is dissipated through nonradiative processes [46, 47]. Isolated metallic nanotubes which have no band gap have an efficient nonradiative recombination pathway, as an excited electron-hole particle can relax to the ground state through a series of transitions mediated by acoustic phonons. As a result, excitons have short lifetimes and the quantum yield of a metallic nanotube is effectively zero [47–49]. The exciton relaxation rate of 10^{11} s^{-1} was measured in isolated CNTs by Wang *et al* [50]. Federspiel *et al* [51] attributed the energy transfer between CdSe/CdS/ZnS NCs and bare graphene to a nonradiative Förster-type resonant energy transfer (FRET) with the frequency of $\sim 6 \times 10^8$ Hz. The same conclusion is shared by Biju *et al* [52] for systems with conjugated CdSe-ZnS QDs and single-wall CNTs. Fluorescence decay measurements may include apart from CT a dominant energy transfer process that leads to very short time constants. Unlike these experiments, the photo-gating effect measured in this study provides a reliable estimation for the temporal characteristics of CT in SC-NCs/CNT devices.

To find any dependence of the LICT on the SC-NCs' sizes, we consider three more combinations of small-bandgap CNT and different CdSe/CdS (core/shell) nanoparticles. The NCs differ in their dimensions (diameter, thickness) as well as in their dimensionality (1D sNRs and 0D QDs). Table 1 presents the

Table 1. CT—fitting parameters. The data presented in the table is the average of the parameters: $<\tau_1>$ (independent for $V_{GG} < 0$), and C_1 for a selection of discrete V_{GG} values, applied during the LICT measurements. L—the NCs length, d—the NCs diameter (see table S2 of the SI).

	NCs size (nm)	Shell thickness (nm)	τ_1 (s)	C_1, −2 V (V)	C_1, −0.9 V (V)	C_1, 0 V (V)
QDs	$d = 3.3$	0.25	9.54	1.91	1.40	0.87
sNRs_A	$L = 30$, $d = 4$	0.45	13	1.49	0.89	0.5
sNRs_B	$L = 65$, $d = 3.5$	0.2	6.11	1.03	0.53	0.25
sNRs_C	$L = 80$, $d = 3.6$	0.1	3.59	0.76	0.50	0.15

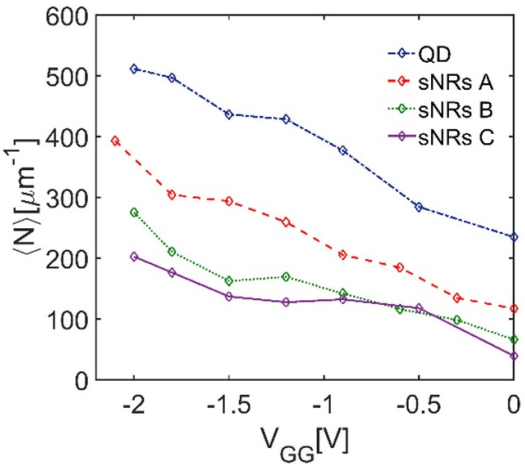

Figure 7. Density of trapped charge within the different NCs at the end of the LICT period. The data presented are the average number of charges <N> (holes) trapped in the NCs per a 1 μm length. The different curves are attributed to the various types of NCs, and the charge density is presented as a function of the applied V_{GG} during the LICT measurements.

parameters' averages extracted from fitting the data of all the different measurements according to equation (1):

The value of C_1, which corresponds to the LICT magnitude is inversely proportional to the NCs size. This is opposite to previous publications which incorporated DWCNT, CdSe QDs, and MTH linker [32, 33]. This difference may originate from the variation of the density of sNRs/QDs coverage. In our devices, the coverage of sNRs_A around the CNTs is typically denser than sNRs_B. Unfortunately, in devices that incorporate QDs and CNT (called QDs in table 1), the QDs are too small to be detected in a SEM scan. The typical-time constants τ_1, show a direct relation to the sNRs size and to the shell thickness (around the seed). The relatively small size-variation of the sNRs seeds in our study prevents us from drawing strong conclusions regarding the seed-size effect on the LICT (described for instance by Zang *et al* [53]). However, we observe that τ_1 is directly correlated to the CdS shell thickness around the seed (the shells thickness goes as: sNRs_A = 0.45 nm > QDs = 0.4 nm > sNRs_B = 0.2 nm > sNRs_C = 0.1 nm). This is consistent with a thinner barrier that assists the core electrons to tunnel through the sNR's shell and may suggest that the majority of the detected LICT originates from the charge in the CdSe core. Using equation (2) we can estimate the density of charge accumulated on the different NCs. Figure 7 depicts the effect of V_{GG} on the amount of (positive) charge accumulated in the different NCs at the end of the LICT period. The presented data are the average of accumulated charge in the NCs, where for negative V_{GG}, $\langle N \rangle$ stands for the number of holes trapped in the NCs per 1 μm length. The average is calculated over two or three devices for each CNT-NCs type.

From SEM images, we roughly estimate ~150 sNRs_A per 1 μm length involve in the LICT, results in a (V_{GG} dependent) charge of 1–3 holes per sNR.

4.2. Charge recovery

A large amount of charge remaining stored in the NCs at the end of the illumination cycle raises a major interest in charge retention, how quickly it disappears, and to what extent. We investigate this charge recovery process by applying one minute 'write' (illumination) pulse under fixed bias and V_{GG}, followed by a long period in which we relax the V_{GG} to 0 V and turn off the light while keeping the bias as is and monitoring the current through the CNT. We probe the I_{DS} with 'read' V_{GG}-pulses (see figure 2(b) in the experimental methods section) and employ the same data analysis as in the charge-transfer measurements section and

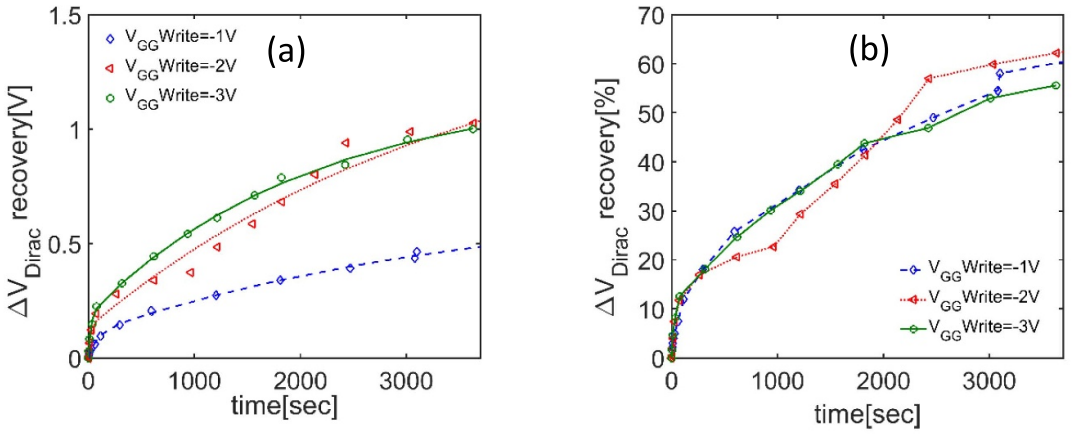

Figure 8. $\Delta V_{\mathrm{Dirac}}$ temporal recovery is measured after 60 s of LICT period (illumination), for sNRs_A and small band gap CNT device, at $T = 290$ K and N_2 atmosphere. (a) Temporal dependence of the $\Delta V_{\mathrm{Dirac}}$ recovery. Raw data are depicted by blue diamonds, red triangles, and green circles for the charge-recovery after the LICT period under $V_{\mathrm{GG}} = -1, -2, -3$ V, respectively. The fitting of the data to equation (5) is presented by lines with matching colors. (b) The temporal recovery of $\Delta V_{\mathrm{Dirac}}$ is presented as a percentage of the initial $\Delta V_{\mathrm{Dirac}}$ at the end of the 'writing stage'.

convert the I_{DS} evolution into temporal dependence of $\Delta V_{\mathrm{Dirac}}$. Figure 8(a) depicts the temporal dependence of $\Delta V_{\mathrm{Dirac}}$ recovery behavior of a device that comprises CNT and sNRs_A for a set of measurements performs under N_2 atmosphere at room temperature. A substantial recovery is observed after one hour. Contrary to the LICT described earlier, the dynamic of $\Delta V_{\mathrm{Dirac}}$ recovery shows poor agreement to a single exponential model. However, an excellent agreement is found when one considers two charge recovery processes with different relaxation times as described by the biexponential kinetic equation of the following form:

$$\mathrm{Fit}_2 = C_1 \cdot \left(1 - e^{-\left(t/\tau_1\right)}\right) + C_2 \cdot \left(1 - e^{-\left(t/\tau_2\right)}\right) \tag{5}$$

where, C_1 and C_2 correspond to the magnitude of $\Delta V_{\mathrm{Dirac}}$, and τ_1 and τ_2 are the temporal characteristic timescale describing two distinct 'fast' and 'slow' charge recovery processes. The fitting of $\Delta V_{\mathrm{Dirac}}$ temporal recovery to equation (5) is depicted in figure 8(a) by colored lines (dashed, dotted, and full for measurements after 'write' at $V_{\mathrm{GG}} = -1, -2$, and -3 V, respectively) with matching colors to the raw data. The parameters extracted from the fitting reflect a mix of 'fast' and 'slow' charge-recovery processes, with approximately two orders of magnitude difference in their time constants. There is no clear dependence of the time constants on the V_{GG} value during the 'writing' stage, nor on the amount of the charge stored in the sNRs at the end of the writing cycle. In general, the magnitude of the charge recovery ($\propto \Delta V_{\mathrm{Dirac}}$) is higher for the larger initial charge stored in the sNRs (which scales according to the 'writing voltage'). Surprisingly, when drawing the recovery percentage relative to the initial charge stored in the sNRs at the end of the 'writing stage' the three curves for the different 'writing voltages' almost collapse to a single curve (see figure 8(b)). For this specific device, over 50% of the initial charge was recovered after one hour. This was the largest charge-recovery percentage that we have measured, and evidently, after one hour the $\Delta V_{\mathrm{Dirac}}$ recovery process is yet to saturate (figure 8(a)).

Figure 9(a) presents the parameters extracted from fitting equation (5) to the data depicted in figure 8(a). The average of the time constants, for fast and slow $\Delta V_{\mathrm{Dirac}}$-recovery processes presented in figure 9(a), are $\langle \tau_1 \rangle \approx 40$s, $\langle \tau_2 \rangle \approx 3100$s, respectively. The magnitude of the slow recovery process (C_2) is 5–10 times larger than the magnitude of the fast recovery process (C_1). Figure 9(b) depicts the fitting parameters of $\Delta V_{\mathrm{Dirac}}$ recovery measured on another device comprise SC-CNT and the same sNRs_A. The sum of the $\Delta V_{\mathrm{Dirac}}$ recovery parameters ($C_1 + C_2$) is comparable to the one in figure 9(a). The averages of the time constants for the fast and slow recovery processes in figure 9(b) are almost twice as large with respect to figure 9(a) and found to be $\langle \tau_1 \rangle \approx 65$ s, $\langle \tau_2 \rangle \approx 6100$ s, respectively. The reason for the large difference in the temporal characteristics of the two charge-recovery processes is not clear. We speculate that it may be explained by a 'double-layer recovery' hopping path. The fast recovery process reflects electrons tunneling from the CNT and recombining with excess holes in the sNRs which are in direct contact with the CNT. The slow recovery process includes charge hopping from sNRs in the first layer into adjacent sNRs which are not in direct contact with the CNT. Moreover, we observed that the temporal dependence of $\Delta V_{\mathrm{Dirac}}$-recovery is almost

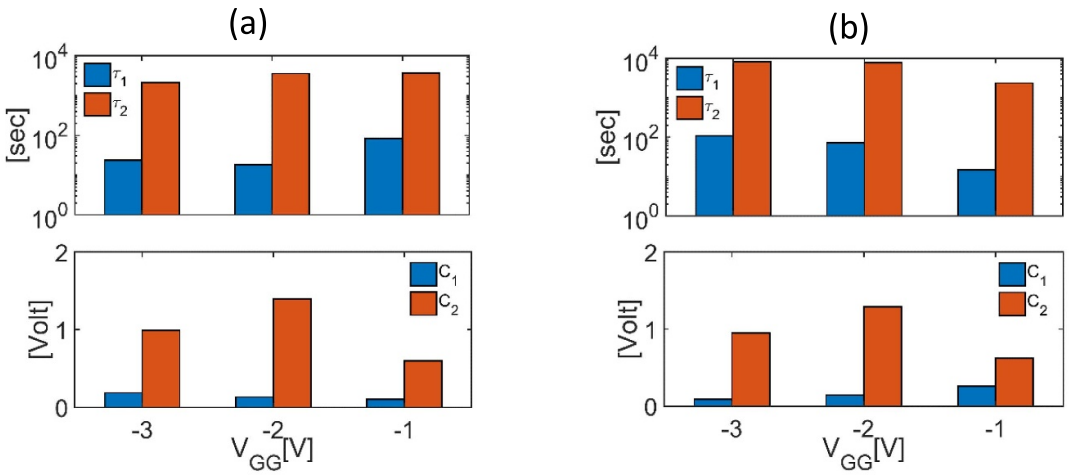

Figure 9. Fitting ΔV_{Dirac}-recovery to equation (5). (a) Fitting parameters corresponding to the data presented in figure 8(a) (small bandgap CNT). The top panel depicts the temporal dependence of the two distinct processes which contribute to ΔV_{Dirac}-recovery. The 'fast' process described by τ_1 and C_1, is approximately two orders of magnitude faster than the 'slow' process characterized by τ_2 and C_2. The bottom panel displays C_1 and C_2, which are the contribution of each recovery process (fast or slow) to the magnitude of ΔV_{Dirac}-recovery. (b) Fitting parameters corresponding to measurements performed on the device of sNRs_A combined with SC-CNT. The top panel presents the fast and slow temporal characteristics parameters, τ_1, and τ_2 with approximately two orders of magnitude difference. The bottom panel presents the recovery-magnitude parameters C_1 and C_2.

Table 2. Recovery—time constants: τ_1 and τ_2 are the typical recovery time constants for the 'fast' and 'slow' recovery processes, respectively. The recovery measurements were performed immediately after LICT under different V_{GG} values (−1, −2, −3 V).

NCs	τ_1 −1 V, (s)	τ_1 −2 V, (s)	τ_1 −3 V, (s)	τ_2 −1 V, (s)	τ_2 −2 V, (s)	τ_2 −3 V, (s)
QDs	67.8	45.6	37.3	2.84×10^3	2.16×10^3	2.24×10^3
sNRs_A	41.56	36.34	53.03	2.50×10^3	4.52×10^3	4.67×10^3

Table 3. Recovery magnitude: C_1 and C_2 are the recovery magnitude associated with the 'fast' and 'slow' recovery processes, respectively. The recovery measurements were performed immediately after LICT under different V_{GG} values (−1, −2, −3 V).

NCs	C_1 −1 V, (V)	C_1 −2 V, (V)	C_1−3 V, (V)	C_2 −1 V, (V)	C_2 −2 V, (V)	C_2−3 V, (V)
QDs	0.146	0.302	0.286	0.302	0.702	0.503
sNRs_A	0.17	0.16	0.22	0.53	0.73	0.96

unaffected by the DOS in the small bandgap CNTs. However, if the LICT shifts the Fermi energy deep into the bandgap of a SC-CNT, the recovery process slows down dramatically. This is presented in figure 9(b), where at the end of the LICT interval for $V_{\text{GG}} = -2$ or −3 V, E_{F} is situated well inside the CNT's bandgap (due to substantial n-doping). Both τ_1 and τ_2 are over three times larger, compared to the case at the end of the LICT period under $V_{\text{GG}} = -1$ V, where E_{F} is situated closer to the edge of the valance energy band (due to lower n-doping).

We apply the same ΔV_{Dirac}-recovery measurements on a set of devices, where CdSe/CdS (core/shell) QDs replace sNRs_A. A comparison between devices incorporating sNRs_A and QDs (three devices of each type) are presented in the following tables which include the averages of the extracted parameters using equation (5), as well as the percentage of the charge recovery.

Table 2 shows comparable recovery time-constants for QDs and sNRs_A devices which suggest that the size of the shell is irrelevant for the recovery process and that most of the charge in the NC is located in its core. In both types of devices there exist two distinct recovery processes, characterized by time constants two orders of magnitude apart. From table 3 we calculate the recovery-magnitude ratio of the 'fast' and 'slow' process, C_2/C_1. For the sNRs_A devices $C_2/C_1 \approx 3$–4, while for QDs devices $C_2/C_1 \approx 2$. These ratios indicate a more substantial 'second layer' in the case of sNRs_A compared to the QDs. Hence, despite having analogous time constants, the 'fast' recovery of sNRs_A is responsible for a significantly lower portion of the charge recovery compared to the QDs. Using our 'double-layer' recovery model, this can be explained by the difference in the coverage of the CNTs by the NCs. The QDs are densely packed along the CNT, with relatively diluted '2nd layer' compared to the sNRs_A, which has fewer NCs attached to the CNT compared to the QDs (due to their size). However, each '1st layer' sNRs is in contact with a few other sNRs which

Table 4. Recovery percentage: The percentage is calculated as ($\Delta V_{\mathrm{Dirac}}$—recovery after 60 min)/($\Delta V_{\mathrm{Dirac}}$ at the end of the LICT sequence).

NCs	Rec −1 V, (%)	Rec −2 V, (%)	Rec −3 V, (%)
QDs	21.8	27.4	30
sNRs_A	49	42	37

constitute the '2nd layer'. Hence, for the QDs a significant part of the charge recovery is associated with direct tunneling to the CNT, whereas for the sNRs_A this recovery channel is less dominant. Table 4 presents an opposite tendency for the charge-recovery percentage as a function of the 'charging voltage' (V_{GG} during the LICT) between the two types of NCs. The data in table 4 also emphasize the slightly longer charge retention for the QDs with respect to the sNRs_A. This may result from charge occupying traps inside the CdS shell or CdSe/CdS interface [54–56], which are more abundant for larger sNRs_A. This property may play an important role in the future generation of electro-optic memory cells.

5. Summary

We present a hybrid opto-electronic device that comprises single CNT and CdSe/CdS—core/shell NCs in a field-effect transistor geometry. Nano-liter droplets of SC-NCs solution were drop-casted on top of the CNT without any CNT functionalization or resist residues. We measure and characterize the effect of different gate voltages stress—V_{GG} (both negative and positive) on the LICT between the CNT and the NCs. Surprisingly, the negative-LICT which was reported in several publications (overall electrons transfer from NCs to CNT) is not exclusive and positive LICT (net holes transfer from the NCs to the CNT) also appears for sufficient high positive V_{GG}. We specify a correlation between I_{DS} measurement during LICT and $\Delta V_{\mathrm{Dirac}}$ and use it to extract the charge accumulated in the NCs (charge transferred to the CNT). The principal contributors to the LICT processes were qualitatively explained and presented by an energy-bands alignment model. The effect of LICT on the I_{DS} can be misleading since it depends on both the LICT type (positive or negative) as well as on the CNT's transfer characteristics and the applied gate voltage. Hence, to measure the dynamics of the LICT we translated the I_{DS} evolution during the 'light on' period, to a shift in the Dirac-point voltage ($\Delta V_{\mathrm{Dirac}}$). The $\Delta V_{\mathrm{Dirac}}$ vs time for negative-LICT was fitted to an exponential dynamic-equation, while positive-LICT (although substantial) was noisy, non-monotonous and allowed for only limited impression on its dynamics and V_{GG} dependence. Under negative V_{GG}, the LICT temporal characteristics of the sNRs_A ($d = 4$ nm, $L = 30$ nm) is almost unaffected by the V_{GG} variation and is estimated to be 13 s. The magnitude of the CT increases (almost) linearly with the magnitude of V_{GG}. The amount of charge occupying each sNR at the end of the LICT is V_{GG}-dependent and estimated to be between 1–3 holes (for $V_{\mathrm{GG}} = 0$ V to $V_{\mathrm{GG}} = -2$ V, respectively).

We measure and compare the LICT process between CNTs and four different types of sNCs. The temporal characteristic has both a direct correlation to the CdS thickness around the CdSe core (thinner shell around core $\leqslant$ faster charging) and is inversely proportional to the sNRs size. The LICT magnitude shows an inverse relation to the NCs size (but this parameter may be also related to the sNCs coverage density). We further investigate the charge retention in the sNCs and propose a recovery model that considers CNT coverage with two layers of sNCs. We compare a set of devices comprise of two different types of sNCs and found that CdSe/CdS QDs ($d = 3.3$ nm) retain their charge longer than sNRs_A ($d = 4$ nm, $L = 30$ nm). Following a LICT sequence, the charge recovery process was characterized by a combination of two slow and fast temporal processes with two different time scales. For the fast process, $\tau_1 \sim 45$ s while the slow process is characterized by τ_2 of more than 45 min. These two distinct recovery processes are related to recovery from the 1st and 2nd NCs layers, respectively.

In conclusion, this study presents the influence of gate-voltage and sNCs-size on LICT between NCs and CNTs. The model and data processing presented here may be utilized for electrically analyzed CT and electrostatic correlation of various hybrid devices. Furthermore, can assist in the optimization and control of LICT processes in hybrid nanostructures, thus improving the future performance of optoelectronic devices.

Data availability statement

The data that supports the findings of this study are available within the article and its supplementary material.

Acknowledgments

This study was supported by the MOST (Grant No. 3-14678), and the Russell Berrie Nanotechnology Institute. The work made use of the Micro Nano Fabrication Unit at the Technion. G Z acknowledges support by the Russell Berrie scholarships.

Supporting information (SI)

The SI includes a description of the synthesis and the geometry of the CdSe/CdS nanocrystals used in this work. As well as a presentation of the translation procedure used to convert I_{DS} vs. time to ΔV_{Dirac} vs. time, and a description of the light-source spectra used throughout the measurements.

ORCID iDs

Adam K Budniak https://orcid.org/0000-0001-7073-8279
Hossam Haick https://orcid.org/0000-0002-2370-4073
Yuval E Yaish https://orcid.org/0000-0001-7997-5457

References

[1] Cao Y, Cong S, Cao X, Wu F, Liu Q, Amer M R and Zhou C 2017 Review of electronics based on single-walled carbon nanotubes *Top. Curr. Chem.* **375** 1–36
[2] Talapin D V, Lee J S, Kovalenko M V and Shevchenko E V 2010 Prospects of colloidal nanocrystals for electronic and optoelectronic applications *Chem. Rev.* **110** 389–458
[3] Omogo B, Aldana J F and Heyes C D 2013 Radiative and nonradiative lifetime engineering of quantum dots in multiple solvents by surface atom stoichiometry and ligands *J. Phys. Chem.* C **117** 2317–27
[4] Maity P and Ghosh H N 2019 Strategies for extending charge separation in colloidal nanostructured quantum dot materials *Phys. Chem. Chem. Phys.* **21** 23283–300
[5] Kagan C R, Lifshitz E, Sargent E H and Talapin D V 2016 Building devices from colloidal quantum dots *Science* **353** aac5523
[6] Reiss P, Protière M and Li L 2009 Core/shell semiconductor nanocrystals *Small* **5** 154–68
[7] Yuan C T, Wang Y G, Huang K Y, Chen T Y, Yu P, Tang J, Sitt A, Banin U and Millo O 2012 Single-particle studies of band alignment effects on electron transfer dynamics from semiconductor hetero-nanostructures to single-walled carbon nanotubes *ACS Nano* **6** 176–82
[8] Eshet H, Grünwald M and Rabani E 2013 The electronic structure of CdSe/CdS core/shell seeded nanorods, type-I or quasi-type-II *Nano Lett.* **13** 5880–5
[9] Deka S *et al* 2009 CdSe/CdS/ZnS double shell nanorods with high photoluminescence efficiency and their exploitation as biolabeling probes *J. Am. Chem. Soc.* **131** 2948–58
[10] Sonnichsen C D, Kipp T, Tang X and Kambhampati P 2019 Efficient optical gain in CdSe/CdS dots-in-rods *ACS Photonics* **6** 382–8
[11] Talapin D V, Koeppe R, Götzinger S, Kornowski A, Lupton J M, Rogach A L, Benson O, Feldmann J and Weller H 2003 Highly emissive colloidal CdSe/CdS heterostructures of mixed dimensionality. *Nano Lett.* **3** 1677–81
[12] Landi B J, Castro S L, Ruf H J, Evans C M, Bailey S G and Raffaelle R P 2005 CdSe quantum dot-single wall carbon nanotube complexes for polymeric solar cells *Sol. Energy Mater. Sol. Cells* **87** 733–46
[13] Olek M, Büsgen T, Hilgendorff M and Giersig M 2006 Quantum dot modified multiwall carbon nanotubes *J. Phys. Chem.* B **110** 12901–4
[14] Carey G H, Abdelhady A L, Ning Z, Thon S M, Bakr O M and Sargent E H 2015 Colloidal quantum dot solar cells *Chem. Rev.* **115** 12732–63
[15] Soltani R, Katbab A A and Ameri T 2017 Recent developments in quantum dots/CNT co-sensitized organic solar cells *J. Mater. Sci. Eng.* **6** 3
[16] Yang J, Lee J, Lee J and Yi W 2019 Improving charge collection from colloidal quantum dot photovoltaics by single-walled carbon nanotube incorporation *ACS Appl. Mater. Interfaces* **11** 33759–69
[17] Li W, He L, Zhang J, Li B, Chen Q and Zhong Q 2019 Anchoring spinel MnCo2S4 on carbon nanotubes as efficient counter electrodes for quantum dot sensitized solar cells *J. Phys. Chem.* C **123** 21866–73
[18] Udorn J, Hou S, Li C, Hatta A and Furuta H 2017 CdSe/ZnS quantum dot (QD) sensitized solar cell utilizing a multi-walled carbon nanotube photoanode on a stainless steel substrate *Int. J. Electrochem. Sci.* **12** 3814–25
[19] Kim Y K and Park H 2011 Light-harvesting multi-walled carbon nanotubes and CdS hybrids: application to photocatalytic hydrogen production from water *Energy Environ. Sci.* **4** 685–94
[20] Wang Z, Wang J, Li L, Zheng J, Jia S, Chen J, Liu B and Zhu Z 2017 Fabricating efficient CdSe-CdS photocatalyst systems by spatially resetting water splitting sites *J. Mater. Chem.* A **5** 20131–5
[21] Li X, Jia Y and Cao A 2010 Tailored single-walled carbon nanotube-CdS nanoparticle hybrids for tunable optoelectronic devices *ACS Nano* **4** 506–12
[22] Shim H C, Jeong S and Han C S 2011 Controlled assembly of CdSe/MWNT hybrid material and its fast photoresponse with wavelength selectivity *Nanotechnology* **22** 165201
[23] Raz L S, Sachyani Keneth E, Jang Y, Shapiro A, Cohen E, Yochelis S, Lifshitz E, Magdassi S and Paltiel Y 2019 Simple fabrication of SWIR detectors based on wet deposition of carbon nanotubes and quantum dots *Sens. Actuators* A **295** 469–73
[24] Sreejith S, Hansen R, Joshi H, Kutty R G, Liu Z, Zheng L, Yang J and Zhao Y 2016 Quantum dot decorated aligned carbon nanotube bundles for a performance enhanced photoswitch *Nanoscale* **8** 8547–52
[25] Wang L, Niu M and Wu Z 2009 *In situ* growth of CdSe/CdS quantum dots inside and outside of MWCNTs *Curr. Appl. Phys.* **9** 1112–6

[26] Paul R and Mitra A K 2016 Nanocomposites of carbon nanotubes and semiconductor nanocrystals as advanced functional material with novel optoelectronic properties *Functionalized Nanomaterials* (Forman Christian College: InTech) (https://doi.org/10.5772/66218)
[27] Shafran E, Mangum B D and Gerton J M 2010 Energy transfer from an individual quantum dot to a carbon nanotube *Nano Lett.* **10** 4049–54
[28] Si H Y, Liu C H, Xu H, Wang T M and Zhang H L 2009 Shell-controlled photoluminescence in CdSe/CNT nanohybrids *Nanoscale Res. Lett.* **4** 1146–52
[29] Abouelsayed A, Anis B, Okasha A, Ali A M, Elhotaby W and Khalil A S G 2018 Preparation, characterization, and spectroscopy study on CdSe quantum dots linked to multi-walled carbon nanotubes *Mater. Chem. Phys.* **203** 1–8
[30] Tang Y *et al* 2018 Significant enhancement of single-walled carbon nanotube based infrared photodetector using PbS quantum dots *IEEE J. Sel. Top. Quantum Electron.* **24** 1–8
[31] Konstantatos G, Badioli M, Gaudreau L, Osmond J, Bernechea M, De Arquer F P G, Gatti F and Koppens F H L 2012 Hybrid graphene–quantum dot phototransistors with ultrahigh gain *Nat. Nanotechnol.* **7** 363–8
[32] Wang L *et al* 2015 Probing the dependence of electron transfer on size and coverage in carbon nanotube-quantum dot heterostructures *J. Phys. Chem.* C **119** 26327–38
[33] Zhu Y, Zhou R, Wang L, Wong S S and Appenzeller J 2017 Utilizing electrical characteristics of individual nanotube devices to study the charge transfer between CdSe quantum dots and double-walled nanotubes *ACS Energy Lett.* **2** 717–25
[34] Robel I, Bunker B A and Kamat P V 2005 Single-walled carbon nanotube-CdS nanocomposites as light-harvesting assemblies: photoinduced charge-transfer interactions *Adv. Mater.* **17** 2458–63
[35] Yu K, Lu G, Chen K, Mao S, Kim H and Chen J 2012 Controllable photoelectron transfer in CdSe nanocrystal-carbon nanotube hybrid structures *Nanoscale* **4** 742–6
[36] Bareket L *et al* 2014 Semiconductor nanorod−carbon nanotube biomimetic films for wire-free photostimulation of blind retinas *Nano Lett.* **14** 6685–92
[37] Weaver J E, Dasari M R, Datar A, Talapatra S and Kohli P 2010 Investigating photoinduced charge transfer in carbon nanotube-perylene- quantum dot hybrid nanocomposites *ACS Nano* **4** 6883–93
[38] Shlafman M, Tabachnik T, Shtempluk O, Razin A, Kochetkov V and Yaish Y E 2016 Self aligned hysteresis free carbon nanotube field-effect transistors *Appl. Phys. Lett.* **108** 163104
[39] Dehnel J, Barak Y, Meir I, Budniak A K, Nagvenkar A P, Gamelin D R and Lifshitz E 2020 Insight into the spin properties in undoped and Mn-doped CdSe/CdS-seeded nanorods by optically detected magnetic resonance *ACS Nano* **14** 13478–90
[40] Wu K, Hill L J, Chen J, McBride J R, Pavlopolous N G, Richey N E, Pyun J and Lian T 2015 Universal length dependence of rod-to-seed exciton localization efficiency in type I and quasi-type II CdSe@CdS nanorods *ACS Nano* **9** 4591–9
[41] Rainò G, Stöferle T, Moreels I, Gomes R, Kamal J S, Hens Z and Mahrt R F 2011 Probing the wave function delocalization in CdSe/CdS dot-in-rod nanocrystals by time-and temperature-resolved spectroscopy *ACS Nano* **5** 4031–6
[42] She C, Demortière A, Shevchenko E V and Pelton M 2011 Using shape to control photoluminescence from CdSe/CdS core/shell nanorods *J. Phys. Chem. Lett.* **2** 1469–75
[43] Wu K, Rodríguez-Córdoba W E, Liu Z, Zhu H and Lian T 2013 Beyond band alignment: hole localization driven formation of three spatially separated long-lived exciton states in CdSe/CdS nanorods *ACS Nano* **7** 7173–85
[44] Robin A, Lhuillier E, Xu X Z, Ithurria S, Aubin H, Ouerghi A and Dubertret B 2016 Engineering the charge transfer in all 2D graphene-nanoplatelets heterostructure photodetectors *Sci. Rep.* **6** 1–11
[45] Bansal P, Zhang X, Wang H, Kar P and Yu W W 2020 Charge transfer between lead halide perovskite nanocrystals and single-walled carbon nanotubes *Nanoscale Adv.* **2** 808–13
[46] Nishihara T, Yamada Y, Okano M and Kanemitsu Y 2014 Quantized exciton-exciton recombination in undoped and hole-doped single-walled carbon nanotubes *Jpn. J. Appl. Phys.* **53** 02BD10
[47] Kinder J M and Mele E J 2008 Nonradiative recombination of excitons in carbon nanotubes mediated by free charge carriers *Phys. Rev.* B **78** 155429
[48] Carlson L J, Maccagnano S E, Zheng M, Silcox J and Krauss T D 2007 Fluorescence efficiency of individual carbon nanotubes *Nano Lett.* **7** 3698–703
[49] Wei X *et al* 2020 Photoluminescence quantum yield of single-wall carbon nanotubes corrected for the photon reabsorption effect *Nano Lett.* **20** 410–7
[50] Wang F, Dukovic G, Brus L E and Heinz T F 2004 Time-resolved fluorescence of carbon nanotubes and its implication for radiative lifetimes *Phys. Rev. Lett.* **92** 177401
[51] Federspiel F *et al* 2015 Distance dependence of the energy transfer rate from a single semiconductor nanostructure to graphene *Nano Lett.* **15** 1252–8
[52] Biju V, Itoh T, Baba Y and Ishikawa M 2006 Quenching of photoluminescence in conjugates of quantum dots and single-walled carbon nanotube *J. Phys. Chem.* B **110** 26068–74
[53] Zang H, Routh P K, Alam R, Maye M M and Cotlet M 2014 Core size dependent hole transfer from a photoexcited CdSe/ZnS quantum dot to a conductive polymer *Chem. Commun.* **50** 5958–60
[54] Gómez-Campos F M and Califano M 2012 Hole surface trapping in CdSe nanocrystals: dynamics, rate fluctuations, and implications for blinking *Nano Lett.* **12** 4508–17
[55] Utterback J K, Wilker M B, Brown K A, King P W, Eavesa J D and Dukovic G 2015 Competition between electron transfer, trapping, and recombination in Cds nanorod-hydrogenase complexes *Phys. Chem. Chem. Phys.* **17** 5538–42
[56] Pu C and Peng X 2016 To battle surface traps on CdSe/CdS core/shell nanocrystals: shell isolation versus surface treatment *J. Am. Chem. Soc.* **138** 8134–42